

Modeling ultrafast laser-driven ionization dynamics with Monte Carlo collisional particle-in-cell simulations

Andreas J. Kemp, Robert E. W. Pfund, and Jürgen Meyer-ter-Vehn

Citation: [Physics of Plasmas](#) **11**, 5648 (2004); doi: 10.1063/1.1814367

View online: <http://dx.doi.org/10.1063/1.1814367>

View Table of Contents: <http://scitation.aip.org/content/aip/journal/pop/11/12?ver=pdfcov>

Published by the [AIP Publishing](#)

Articles you may be interested in

[High field terahertz emission from relativistic laser-driven plasma wakefields](#)

[Phys. Plasmas](#) **22**, 103105 (2015); 10.1063/1.4933130

[Improved modeling of relativistic collisions and collisional ionization in particle-in-cell codes](#)

[Phys. Plasmas](#) **19**, 083104 (2012); 10.1063/1.4742167

[2D particle-in-cell simulations of ion acceleration in laser irradiated submicron clusters including field ionization](#)

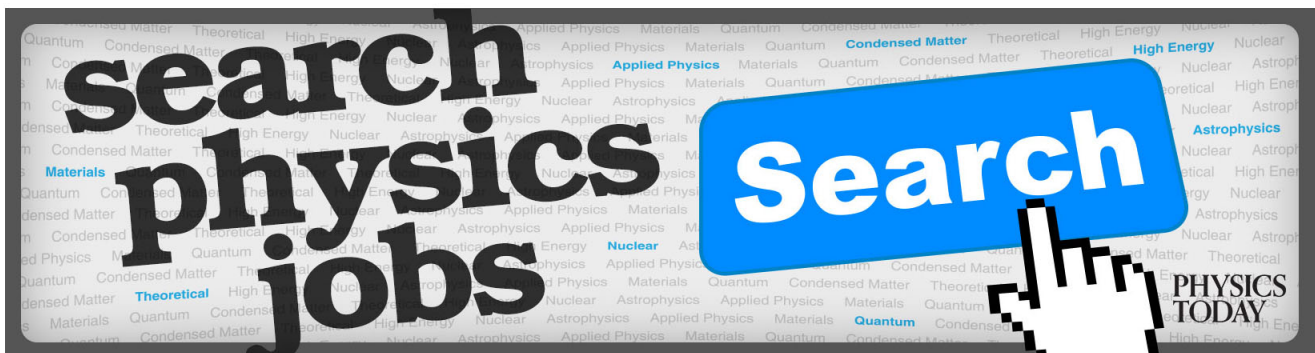
[Phys. Plasmas](#) **19**, 043107 (2012); 10.1063/1.4704791

[Towards a fully kinetic 3D electromagnetic particle-in-cell model of streamer formation and dynamics in high-pressure electronegative gases](#)

[Phys. Plasmas](#) **18**, 093501 (2011); 10.1063/1.3629989

[Integrated kinetic simulation of laser-plasma interactions, fast-electron generation, and transport in fast ignitiona\)](#)

[Phys. Plasmas](#) **17**, 056702 (2010); 10.1063/1.3312825



Modeling ultrafast laser-driven ionization dynamics with Monte Carlo collisional particle-in-cell simulations

Andreas J. Kemp

Department of Physics, University of Nevada, Reno, Nevada 89506

Robert E. W. Pfund and Jürgen Meyer-ter-Vehn

Max-Planck-Institut für Quantenoptik, Hans-Kopfermann-Strasse 1, D-85748 Garching, Germany

(Received 4 March 2004; accepted 15 September 2004; published online 12 November 2004)

Ionization dynamics of cold dense matter induced by ultrashort (<100 fs) laser pulses is studied for intensities at the onset of the relativistic regime by one-dimensional kinetic simulations. As a model we use a particle-in-cell code that includes field and electron collisional ionization, as well as elastic binary Coulomb collisions. As examples for the different ionization mechanisms, we give the spatial and temporal evolution of laser-induced ionization dynamics in helium gas and solid boron targets. Special attention is paid to the quasi-static electric fields at the rear surface of laser-irradiated targets that are important for laser-ion acceleration. © 2004 American Institute of Physics.

[DOI: 10.1063/1.1814367]

I. INTRODUCTION

Ultrashort laser pulses at energies of up to several joules that have become available recently allow detailed studies of ionization dynamics in initially cold matter.^{1,2} While the plasma formation stage is usually not considered in descriptions of long-pulse—i.e., picosecond or nanosecond pulse—experiments, it is a key feature of ultrashort laser interaction, where a significant fraction of the laser-pulse energy goes into the ionization of the target material, and the time scale of the laser pulse is comparable to that of the ionization dynamics itself. There are many scenarios where ionization dynamics plays an important role, for example, ultrafast generation of radiation and the fast-ignitor scheme for inertial confinement fusion.^{3–5} As one particular application, we will discuss the effects of ionization dynamics on the laser-driven acceleration of ions. The latter relies on an electron charge sheath that is formed behind the laser-irradiated target. Since these electrons come from the interaction region at the front, understanding their transport through the ideally nonionized, solid matter is important; it is likely to be affected by ionization dynamics, via electric fields by compensated space charges in regions where little or no return current electrons are available, for example, in insulators.⁶ The ionization-induced pattern in the electron transport will make an imprint on the evolution of the electrostatic sheath field behind the target and become an observable feature of laser-accelerated ion beams.⁷

Here we report on a numerical model for the investigation of ultrafast ionization phenomena in laser-matter interaction that is based on a one-dimensional particle-in-cell (PIC) description and includes field and collisional ionization as well as binary Coulomb collisions.⁸ To demonstrate the capabilities of the model, we apply it to few-cycle pulse laser-matter interaction at the onset of relativistic intensities, i.e., at 10^{17} W/cm² and optical frequencies. There are three principally different descriptions of ionization dynamics and

collisions that are used in the context of laser-plasma interaction. These are the following.

(i) A hydrodynamic approach with a Maxwell solver for the calculation of laser energy deposition in a steep density gradient plasma, such as the MULTI-fs code;⁹ it models the complex-valued dielectric constant based on an interpolation of the electron collision frequency between a cold solid and a hot plasma. With this semiempirical model it reproduces laser absorption in the target and thermal energy transport into the target reasonably well, as long as the laser intensity is nonrelativistic. However, it does not describe the generation and propagation of fast electrons.

(ii) Hybrid Fokker–Planck simulations solving the Langevin equation^{10,11} explicitly follow distribution functions for electrons and ions. This includes a consistent description of nonthermal fast electrons, but can be very expensive in terms of computer time, if no simplifications are made.

(iii) PIC codes have been extended to include ionization and binary collisions by several groups.^{12–14} Our approach differs from previous ones in that (a) our model includes ions as freely movable individual particles that can be either electrically neutral or ionized, rather than using average charge states; electrons and ions undergo binary Coulomb collisions, resulting in energy transfer between various species; (b) our Monte Carlo model for binary collisions¹⁵ does not make any assumption about a particle distribution function, unlike the models in Refs. 11 and 14. In experiments at laser intensities below 10^{16} W/cm² and pulse durations around 1 ps, the actual form of the electron distribution function has been found to have no strong effect on the ionization state of the plasma.¹⁶ This may change at higher laser intensities, when a larger fraction of laser energy is converted into fast, nonthermal electrons.

In the following we will describe our numerical model, and then highlight some key features of laser-matter interaction in a parameter regime where inelastic effects play an important role. As examples we present (1) the interaction of

a short-laser pulse with a helium gas target, in which a beam of fast electrons is generated that oscillates back and forth through the target and causes a quasistatic electric field on the target surfaces; (2) a solid boron foil target, as it might be used in an actual experiment. In both cases we compare the case of an obliquely incident laser beam to normal incidence. Case (2) is instructive with respect to the role of binary Coulomb collisions and collisional ionization in dense targets as compared to gas targets. The fact that elastic binary collisions are included in our simulations allows us to study the onset of the collisional laser plasma interaction regime at high plasma densities and subrelativistic laser intensities ($I\lambda^2 < 10^{18} \text{ W cm}^{-2} \mu\text{m}^2$), where the dynamics can be described by hydrodynamics and where heat transport is mostly diffusive. The aspect of nonlocal versus diffusive heat transport will be discussed in more detail in a later publication.¹⁷

II. MONTE CARLO COLLISIONAL PIC MODEL

Particle-in-cell codes solve the relativistic equations of motion for a large number of particles together with Maxwell's equations on a mesh of cells that is fixed in space.¹⁸ The macroparticles—representing electrons and ions—are accelerated by electric and magnetic fields that are averaged over the cells. Each macroparticle (called “particle” below) in the simulation corresponds to a large number of physical particles in order to make real problems with plasma dimensions of some tens of micrometers and time durations of hundreds of femtoseconds tractable. Our numerical model is based on LPIC,¹⁹ a relativistic and fully electromagnetic PIC code with one spatial and three velocity dimensions for simulating laser-plasma interaction at normal and oblique incidence; the latter is treated by Bourdier's method,²⁰ transforming the target into a moving frame in which the laser is normally incident.

A. Numerical requirements

PIC-Monte Carlo collisional (MCC) simulations that include ionization dynamics require a much higher numerical resolution than “ideal” PIC simulations. This has two reasons; in problems where ionization dynamics plays a significant role, the plasma temperatures are at least temporarily lower than in ideal PIC simulations which assume the targets to be ionized; furthermore, we are mostly interested in targets at solid density where collisional effects become dominant, while ideal PIC simulations can be set up at lower densities and still contain the relevant phenomena. The spatial grid resolution Δx of an ideal PIC simulation is usually the electron Debye length $\lambda_D = v_{th}/\omega_{pe}$, where $v_{th} = \sqrt{kT_e/m_e}$ is the thermal velocity of the electrons with temperature T_e and $\omega_{pe} = (4\pi n_e e^2/m_e)^{1/2}$ is the electron plasma frequency; the time step is fixed by $\Delta t = \Delta x/c$, where c is the speed of light.²¹ As an example, let us apply these guidelines to the case of a $\lambda = 400 \text{ nm}$ wavelength laser pulse interacting with a target at 100-fold overcritical electron density, corresponding to fully ionized solid density boron, compare Sec. IV below. The number of cells per wavelength N_c depends on the assumed temperature of the plasma: at 10 eV one has $N_c = 15\,500$, at 1 keV one has $N_c = 1550$, etc. The time con-

sumption of our model scales approximately linearly with the total number of particles, since the Monte Carlo part of the algorithm consumes $\approx 55\%$ of the resources and the propagation of particles uses more time than the Maxwell-solver for a one-dimensional (1D) geometry. On a Pentium-IV processor at 1 GHz speed, the LPIC-MCC code takes $\approx 1.5 \text{ s}$ per time step with 10^5 particles (and 2000 cells total), as compared to 0.68 s per time step without the MCC module. For the parameters of the problem discussed in Sec. IV below, the total simulation time is roughly 12 h on a single CPU.

The high demands in resolution explain the difficulties using PIC-MCC models for large-scale 2D simulations; a two-dimensional setup that corresponds to the 1D case described above requires a transverse target size of $\approx 30\lambda$ for a realistic laser spot diameter and the longitudinal size of 1λ . Such a simulation would contain at least 10^{10} particles before ionization, meaning 10^{12} bytes of memory and 10^5 s per time step, even neglecting networking activity and the more complex 2D Maxwell solver. This explains the need for massive parallel processing, but even with hundreds of CPUs the costs are high. In reality, however, these requirements can be strongly relaxed because (i) ionization and collision physics occurs on a much slower time scale than the plasma physics, as described in Sec. II C below; (ii) the plasma is fully ionized only when the electron temperature is high; at the beginning of the laser interaction when the plasma is still cold, the ionization degree is small. This works in favor of a lower resolution; (iii) numerical convergence can be achieved at a lower resolution than the Debye scale. From our experience, the minimum length scale that must be resolved by a plasma description to include charge-shielding effects in transport phenomena is the skin length $l_s = c/\omega_{pe}$; since this is roughly two orders of magnitude larger than the Debye length (at an electron temperature of 50 eV), collisional PIC simulations can be performed with reasonable amounts of time and computer memory.²² Nevertheless, it is important to verify the results of an underresolved multidimensional simulation with 1D simulations at a better resolution.

Our model is currently limited to a one-dimensional description, i.e., we assume the plasma to be transversely homogeneous. This naturally excludes effects such as azimuthal magnetic fields and transverse beam widening, which are known to be of importance at high laser intensities.²³ In the case of subrelativistic laser pulses, the 1D assumption can be justified by experiments that have demonstrated the thickness of the directly or indirectly heated target layer of less than $1 \mu\text{m}$ to be significantly smaller than the typical laser focal spot size $\approx 20 \mu\text{m}$.²⁴ Since the net charge and current density of fast electrons in the target is small, we expect no significant widening of the electron cloud that could be caused by transverse electric space-charge fields, or pinching due to inductive magnetic fields as mentioned elsewhere for the case of higher laser intensities.²⁵

Being a mean field description, a standard PIC code neglects collisions and related inelastic processes such as ionization, bremsstrahlung, pair production, just to name a few. Our method to incorporate such processes into LPIC is to add them in a probabilistic Monte Carlo collisional way. In

the simulations presented below, we start with nonionized targets which are ionized during the interaction with the laser pulse. Two different types of ionization processes are implemented: field ionization, i.e., ionization in strong electric fields, and electron collisional ionization. At higher target densities, especially in the case of solid density and at laser intensities of the order 10^{17} W/cm², collisions between plasma particles play an important role as will be described below. For such situations, LPIC includes Coulomb binary collisions.

B. Field ionization

The field-ionization model in LPIC is based on the description of tunnel ionization of complex atoms in alternating electric fields given by Ammosov, Delone, and Krainov²⁶ in the form of Penetrante and Bardsley.²⁷ The ionization rate of an ion at a charge state $Z-1$ in an ac-electric field E_f is then

$$R_i = 6.6 \times 10^{16} \frac{Z^2}{n_{\text{eff}}^{4.5}} \times \left[10.87 \frac{Z^3}{n_{\text{eff}}^4} \frac{E_H}{E_f} \right]^{2n_{\text{eff}}-1.5} \times \exp \left[-\frac{2}{3} \frac{Z^3}{n_{\text{eff}}^3} \frac{E_H}{E_f} \right] (\text{s}^{-1}), \quad (1)$$

where $E_H \equiv m_e^2 e^5 \hbar^{-4} = 5.14 \times 10^{11}$ V/m is the electric field strength between an electron and a proton on the first Bohr orbit of a hydrogen atom, $n_{\text{eff}} = Z / \sqrt{E_{\text{ion}}(\text{eV})/13.6}$ is the effective main quantum number of the ionized electron, and E_{ion} is the ionization potential in eV. Plasma density effects on the field ionization rate are not accounted for. In a given cell, the ionization probability $P_i = \Delta t R_i$ is calculated at each time step for each ion—note that the term ion stands for neutral as well as ionized macroatoms. Depending on the value of a computer-generated random number, the particle is ionized and a corresponding photoelectron is created at the location of the ion and initialized with zero velocity. During the next time step, the electric field separates the two particles.

In order to retain energy conservation throughout the simulation, the ionization energy for a given process $E_{\text{ion}}^{\text{part}}$ is subtracted from the electromagnetic field, i.e., the field energy changes by ΔE_f . This is accomplished by introducing an artificial ionization current \mathbf{j}_{ion} that is added to the current in the cell for only one time step; it is called the virtual ionization current.^{28,29} The ionization current \mathbf{j}_{ion} is directed along the electric field \mathbf{E} , and its magnitude is determined from

$$\int dt \int dV \mathbf{j}_{\text{ion}}(t) \cdot \mathbf{E}(t) = \Delta E_{\text{field}} \equiv E_{\text{ion}}^{\text{part}}. \quad (2)$$

In the PIC algorithm \mathbf{j}_{ion} is added to the physical current in each cell, after charge and current are computed from particle positions and velocities and before the integration of Maxwell's equations. For a high-density material, such as for example, the boron foil discussed below, it may happen that the field-ionization rate predicts more ionization events per time step than energetically possible. In this case, the number of ionization events is limited so that energy is conserved.

C. Electron collisional ionization

With increasing target density, electron collisional ionization becomes more and more important as compared to the field ionization. It will become dominant for solid targets, as shown in Sec. IV. Therefore, electron collisional ionization has also been implemented in LPIC. Ionization starts for all charge states from the energetic ground level. Excited electronic states are not considered at present, neither are recombination processes, see Sec. II C 1 below.

For an electron with velocity v_{el} and $Z-1$ types of ionization processes, corresponding to Z different ion charge states, the total collision ionization frequency is given by

$$\nu_{\text{tot}}(E_{\text{el}}) = v_{\text{el}} \sum_{i=0}^{Z-1} \sigma_i(E_{\text{el}}) n_i(x). \quad (3)$$

Here $n_i(x)$ is the number density of ion charge state i and $\sigma_i(E_{\text{el}})$ is the cross section for the i th ionization process, which can be either interpolated from a table³⁰ or computed via the Lotz formula.³¹ The ionization cross section depends only on the electron kinetic energy $E_{\text{el}} = m_{\text{el}} v_{\text{el}}^2 / 2$. The total collision probability for an electron-ion pair during the time interval Δt is then

$$P_{\text{el}} = 1 - \exp(-\Delta t \nu_{\text{tot}}). \quad (4)$$

In a typical simulation, the collisional-ionization probability P_{el} will be very small since $\Delta t \nu_{\text{tot}} \ll 1$ and there will be no ionization events during most time steps.

To save computational resources, our implementation uses a null collision method.³² A similar algorithm has been used earlier by Vahedi and Surendra.³³ Some aspects of our implementation are (i) locality in space, i.e., colliding electrons and ions are in the same cell, (ii) energy conservation, and (iii) the ability to handle arbitrary ion charge states. In the beginning of a simulation, the maximum value of the $\langle \sigma_i v \rangle$ products for each charge state i is stored, where the brackets stand for an average over a Maxwellian energy distribution. During the simulation, the maximum frequency ν_0 is computed in each time step and each cell as

$$\nu_0 = \max_{v_{\text{el}}} \left\{ \sum_{i=0}^{Z-1} \langle \sigma_i v \rangle n_i \right\} = \sum_{i=0}^{Z-1} n_i(x) \max_{v_{\text{el}}} \{ \langle \sigma_i v_{\text{el}} \rangle \}. \quad (5)$$

It depends only on the number of ions in each cell, but not on individual electron velocities, and determines the maximum number of electrons undergoing a collision as

$$P_0 = 1 - \exp(-\Delta t \nu_0). \quad (6)$$

Next, $P_0 N_{\text{el}}$ electrons are randomly chosen from the total number of N_{el} per cell. The ionization process for each electron is selected using the random number R with a uniform distribution $0 \leq R \leq 1$. Depending on the value of R , the i th possible event is executed:

$$R \leq \frac{\nu_1(E_{\text{el}})}{\nu_0}, \quad (7)$$

$$\frac{\nu_1(E_{el})}{\nu_0} < R \leq \frac{\nu_1(E_{el}) + \nu_2(E_{el})}{\nu_0}, \quad (8)$$

...

$$\sum_{i=0}^{Z-1} \frac{\nu_i(E_{el})}{\nu_0} < R \text{ (null collision)}, \quad (9)$$

where $\nu_i = n_i \nu_{el} \sigma_i$. The last option is a so-called “null” collision in which no event takes place. It stems from our overestimation of the collision frequency when using the maximum value of $\langle \sigma \nu \rangle$ instead of individual electron information.

If the total number of ionization events in one cell $P_0 N_{el} < 1$, e.g., because the time step is too small, no electron is selected for a collision immediately. Instead, the value of $P_0 N_{el}$ is accumulated over several time steps until a collision can take place and the counter is reset. We have checked the effect of locality of the counter on the ionization dynamics in the case study of the boron foil target below, finding that it makes only a small difference if a counter is introduced for each cell, or if there is only one global counter. The main reasons are that (i) mostly subrelativistic electrons are relevant for collisional ionization of low- Z ions. They will not leave the cell before an ionization event takes place; (ii) collisional-ionization events are rather slow compared to the plasma frequency which determines the time step of the PIC code. For example, the maximum electron impact ionization rate of neutral solid boron is $2 \times 10^{-16} \text{ s}^{-1}$,³⁰ it has to be compared to the simulation time step $\Delta t = \Delta x / c$, where Δx is the spatial resolution that is chosen to be similar to the expected value of the Debye length. In our case study, we have used $\Delta t = 1.8 \times 10^{-18} \text{ s}$. This demonstrates the slowness of collisional ionization compared to other plasma processes, motivates the necessity of an accumulated ionization probability, and shows the usefulness of the null-collision method. Since the value of the ionization probability P_0 needs to be computed for each time step, the latter can save a great amount of computational time as compared to a method in which ionization probabilities are computed for each electron individually.

Finally, when an ionization event takes place, the charge state of a randomly chosen ion with the appropriate charge state is changed, and a free electron is created at the position and at rest with respect to the ion. Then the ionization energy is subtracted from the colliding electron by reducing the magnitude of its velocity, while keeping its direction unchanged. We found that it is important to initialize new-born electrons with zero velocities *relative to the ion* because otherwise, ion-acoustic waves are generated that will change the plasma dynamics. An alternative way to initialize electrons is the so-called indirect ionization in which atomic excitation is followed by an autoionization process, leading to a finite initial velocity of the ionized electron; however, this scheme plays only a little role for most low- Z materials.³⁴

1. Recombination

Three-body recombination—the inverse process to electron collisional ionization—dominates over the competing photorecombination at high densities and temperatures below 1000 eV, which are the conditions of interest here.^{35,36} A simple expression for the three-body recombination rate, which typically overestimates the rate at temperatures $> 1 \text{ eV}$, is given by

$$Z_{rec} = b N_e N_+, \quad (10a)$$

where

$$b = \frac{2.6 \times 10^{-41} Z_{eff}^3}{T_{1000 \text{ eV}}^{9/2}} N_e \left(\frac{\text{cm}^3}{\text{s}} \right) \quad (10b)$$

while N_e and N_+ denote electron and ion densities.³⁵ In a boron plasma at solid density with effective charge state $Z_{eff} = 3$ and an electron temperature of 1000 eV, corresponding to the case discussed in Sec. IV below, Eq. (10) yields a recombination rate of $10^{30} \text{ cm}^{-3} \text{ s}^{-1}$. Under the same conditions the impact ionization rate is $\approx 3 \times 10^{38} \text{ cm}^{-3} \text{ s}^{-1}$.³⁰ Similarly, in the helium gas target presented in Sec. III, impact ionization is more than three orders of magnitude faster than its inverse process.

These examples demonstrate that recombination physics can be neglected during the short period of time where matter is intensely heated by the laser or electron heat transport while it is still dense, which is consistent with the scope of our model. Eventually, however, recombination will set in as the plasma loses heat via expansion cooling and radiation; this occurs typically after several laser pulse durations, or after hundreds of femtoseconds, depending on which is longer. That stage of the plasma evolution is not covered here.

D. Binary coulomb collisions

In order to describe the transition from collisionless plasmas to collisional ones, LPIC includes small-angle binary Coulomb collisions following Takizuba and Abe's (TA) model.¹⁵ We have modified their model to treat the collision particle kinetics relativistically correct, as described in Ref. 37. This means that the momenta of any two collision partners are Lorentz-transformed between laboratory and center-of-mass (CM) frame instead of using Galilei transforms, as in TA. Such a fully relativistic treatment of collisions is important for the correct description of intense laser-plasma interaction, as soon as electrons are accelerated to near-light velocity, i.e., when the scaled laser amplitude $a = eE/m\omega c$ reaches $a \approx 1$.

The principles of the binary collision operator will be sketched here only briefly in the most simple case; for more details we refer to Refs. 8, 15, and 38. Collisions are executed in each time step between selected random partners in spatially localized regions that extend over a Debye screening length; these collision cells coincide with the PIC cells. Particles that are located in different cells do not interact. In a $Z=1$ plasma with an even number of electrons and protons in each cell, one first executes intraspecies collisions between particle numbers m and $m+1$ for electrons and pro-

tons, then interspecies collisions between electron number m and proton number m . In each binary collision process, the relative particle velocity $u=|\mathbf{u}|$ in the CM frame is determined and the collision frequency is calculated according to Spitzer's formula³⁹ (in cgs units)

$$\nu_{\alpha\beta} = \frac{4\pi^{3/2} q_\alpha^2 q_\beta^2 \ln \Lambda n_{\alpha\beta}}{m_{\alpha\beta}^2 u^3}, \quad (11)$$

where q_α represents the charge of particle α , $\ln \Lambda$ is the Coulomb logarithm which is assumed to be constant here, $n_{\alpha\beta} = \min(n_\alpha, n_\beta)$, and $m_{\alpha\beta} = m_\alpha m_\beta / (m_\alpha + m_\beta)$ is the reduced mass. The azimuthal scattering angle in the CM frame is determined from a Gaussian distribution with a width $\nu_{\alpha\beta} \Delta t$ that is generated from two uniform random number distributions via the Box-Muller method,⁴⁰ while the poloidal scattering angle ϕ is directly determined from a uniform random number distribution between 0 and 2π . If $\nu_{\alpha\beta} \Delta t > 0.5$, the small-angle scattering assumption of the TA model breaks down and the azimuthal scattering angle is determined from a uniform distribution on the sphere; to do this, $\cos \theta$ is determined from a uniform distribution of random numbers. Finally, the relative velocity vector is rotated by these angles, then transformed back into the laboratory system and added to the scattering particle velocities. We have tested our implementation of the TA model successfully against analytic models for the temperature equilibration of a two-component plasma.⁸

III. CASE STUDY: HELIUM GAS TARGET

A. Normal incidence

As a first simple model system exhibiting the two ionization mechanisms discussed above, we study an initially neutral He gas layer that is irradiated by a short laser pulse. The laser pulse is six laser cycles long with a maximum intensity of $I = 9 \times 10^{16} \text{ W/cm}^2$ at a wavelength $\lambda = 1 \mu\text{m}$, corresponding to a dimensionless amplitude of $a = 0.256$ and a sin-shaped field envelope. The pulse is linearly polarized and normally incident on a 1λ thick He gas layer with a uniform ion density at $n_i = 2 \times 10^{21} \text{ cm}^{-3}$, corresponding to two times overcritical density, where the critical density n_c for a laser frequency ω_L is defined as $n_c = \omega_L^2 m_e / 4\pi e^2$. In our simulation we use 600 cells per wavelength and 100 macroions per cell to resolve the target. For a fully ionized He target, i.e., $n_e = 2n_i$, this resolution corresponds to one Debye length per cell at a temperature of roughly 100 eV. Immediately after the target is ionized, the electron temperature typically exceeds 1 keV; this demonstrates that the numerical resolution is sufficient. The total size of the simulation box is chosen such that no particle reaches the box boundary; its total length is 7λ .

Figure 1 gives the space-time history of the electron density $n_e(x, t)$, the longitudinal electric field $E_x(x, t)$, and ionization events. Time is given in units of laser cycles $\tau \approx 3.3 \text{ fs}$. The laser pulse which comes from $x=0$ reaches the gas layer at $t=3\tau$, and, as soon as the laser intensity in the first half cycle is strong enough at $t=3.25\tau$, field ionization sets in. The pulse propagates with a sharp ionization front through the neutral layer, field ionizing the material up to

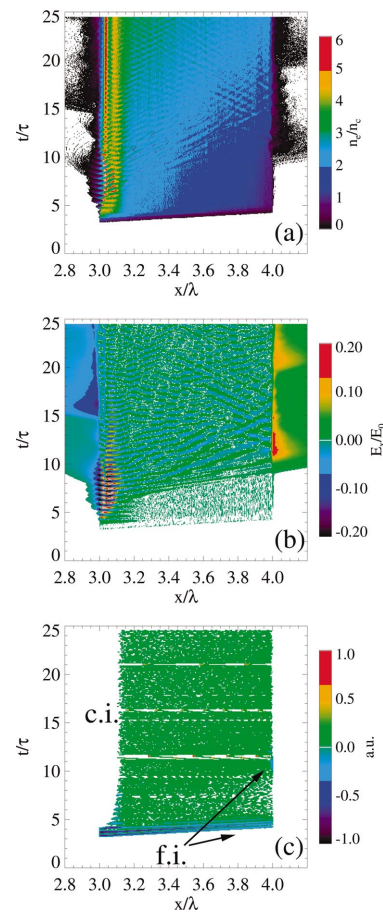


FIG. 1. (Color). Helium target under normal incidence. The laser pulse arrives at the target from the left at $t=3\tau$. (a) Electron density n_e in units of the critical density n_c vs target depth x given in wavelengths λ and time t given in laser periods τ . (b) Longitudinal electric field E_x in units of the laser field $E_0 = 3 \times 10^{12} \text{ V/m}$. (c) Ionization events marked as "f.i." (field ionization) or as "c.i." (collisional ionization). The color scale corresponds to the number of ionization events: green corresponds to a few c.i. events, while red corresponds to strong c.i.; white areas indicate no ionization events; darker shades of blue correspond to larger numbers of f.i. events.

He^{+2} at the front surface; inside the target the pulse can field ionize only up to He^+ . Here collisional ionization dominates at later times.

The space-time history of the electron density, as shown in Fig. 1(a), can also serve as a plot of the ion charge state, when divided by the neutral ion density. More detailed plots of the charge state distribution are shown in Fig. 2 below. The field-ionization thresholds for helium are $\approx 10^{11}$ and $3 \times 10^{11} \text{ V/m}$, respectively. Inside the target at $x > 3.1\lambda$, the electric field is not strong enough to ionize up to He^{+2} ; instead, collisional ionization sets in, mostly in the left part of the target. The horizontal regions with a small, but spatially localized number of collisional-ionization events, for example at $t=12\tau$, are a numerical artifact that belongs to the accumulation of probabilities for collisional ionization. This occurs at low material densities where ionization rates are very small, and changes the final ionization degree of the target by not more than 10%, compare Sec. II C.

The rear side of the target does not interact directly with the laser pulse. Instead, the light pressure of the reflected laser pulse excites plasma waves and generates fast electrons

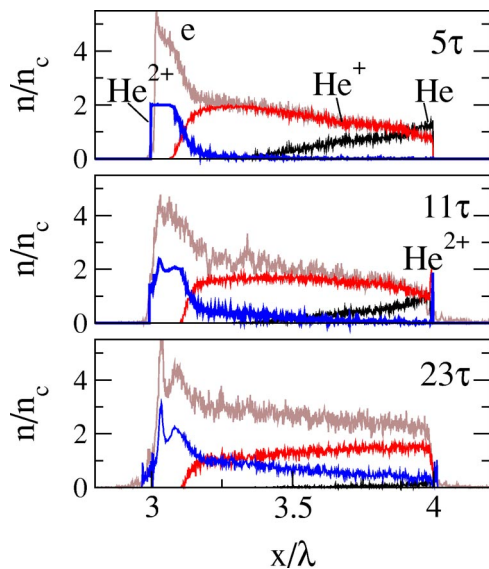


FIG. 2. (Color online). Helium target under normal incidence. Charge state distribution vs target depth in the He layer at different times.

at the front of the target via the $\mathbf{j} \times \mathbf{B}$ force,²¹ while light is reflected at the critical density, where $n_e = n_c$, and electrons with $v_e \approx 0.3c$ pass deeper into the target and then enter the partially ionized region. Here these electrons build up longitudinal space-charge separation fields, clearly visible in the space-time plot, Fig. 1(b), starting at $x = 3.2\lambda$ and $t = 7.5\tau$. These fields are strong enough to ionize the material up to He^+ . When fast electrons finally exit at the rear surface at $x = 4.0\lambda$ and $t = 9.25\tau$, an even stronger electric field builds up that leads to a thin layer of He^{2+} at the rear surface, which is clearly visible in Fig. 2. The corresponding field-ionization events can be seen in Fig. 1(c), as indicated by the upper arrow.

Figure 2 gives a more detailed picture of the ionization degree of the He versus target depth at three times: at $t = 5\tau$, at $t = 11\tau$ when the longitudinal electric field at the rear target surface reaches its maximum, and at $t = 23\tau$, long after the laser pulse is over. Even after the laser-pulse maximum has passed through the target at $t = 5\tau$, only a small fraction of the gas at the rear side of the target is fully ionized while the front of the target ($3.0\lambda < x < 3.1\lambda$) has been ionized to He^{2+} during the second half cycle of the pulse, i.e., before $t = 5\tau$. Although only 0.1% of the total pulse energy is used up for ionization, the first half cycle of the laser pulse loses about 11% of its energy due to ionization. Note that the apparent decrease in the density of He^{2+} ions at the rear target surface between $t = 11\tau$ and 23τ is due to ion expansion into vacuum, driven by the longitudinal electric field shown in Fig. 1.

In a gas target at an electron density of 10^{21} cm^{-3} and thermal electron velocities of $v \approx 0.1c$, the maximum impact ionization cross section for He of $\sigma \leq 10^{-17} \text{ cm}^2$ yields an ionization rate of 10^{13} s^{-1} . This is small compared to the field-ionization rate, which can be as large as 10^{17} s^{-1} . This is the reason why collisional-ionization events play only a minor role compared to field-ionization events, compare Fig. 1(c). There is a large number of field-ionization events as the laser pulse passes through the initially neutral gas, shown in

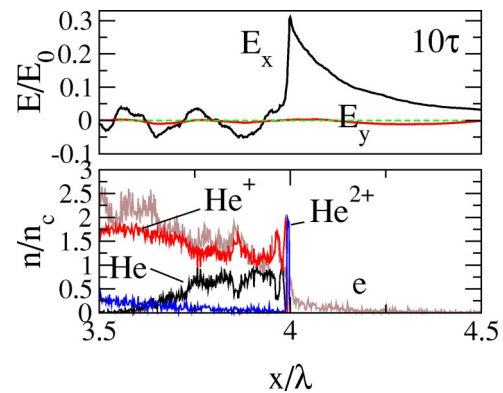


FIG. 3. (Color online). Helium target under oblique incidence $\alpha = 31^\circ$. Snapshots of electric field and charge state distributions vs target depth x in the second half of the target at time $t = 10\tau$ when E_x reaches its maximum at the rear target surface.

dark blue. They are followed only by a small number of collisional-ionization events shown in green. In other words, collisional ionization occurs deep in the target where the laser pulse cannot get after the material ionized. A simulation that corresponds to one just discussed but with no collisional ionization shows that the presence of He^{2+} is exclusively due to collisional ionization. Further, binary collisions at gas densities can be neglected; this has been checked by a corresponding collisionless simulation.

B. Oblique incidence

A distinct feature of intense laser-matter interaction are the quasistatic, longitudinal electric fields on the rear surface of thin foil targets that are generated by laser-accelerated electrons from the front of the target.^{41,42} To make the effect of the electron jets clearly visible, we have performed a simulation with an obliquely incident ($\alpha = 31^\circ$) laser pulse that is otherwise identical to the one discussed above, as is the target. As mentioned above, oblique incidence is treated in LPIC by transforming the target into a moving frame of reference according to Bourdier's method.²⁰ In contrast to normal incidence, there is a component of the electric laser field perpendicular to the target surface and electrons are mainly accelerated via the so-called Brunel effect⁴³ giving a higher laser-to-electron energy coupling efficiency. Although the distinction between normal and oblique incidence is somewhat unrealistic for a gas target, it is useful from an instructional point of view.

Figure 3 shows snapshots of the rear side of the target at $t = 10\tau$. Comparing the three components of the electric field, one can see that inside and behind the target it is mainly of longitudinal nature; the transverse components E_y , which is the laser polarization direction, and E_z are negligibly small. Inside the gas layer, one can identify plasma waves with amplitudes on the order of 10^{11} V/m . The magnitude of the space-charge separation field right at the rear side is $5 \times 10^{11} \text{ V/m}$. It decays behind the target in a space-charge cloud of electrons to $5 \times 10^{10} \text{ V/m}$ over a length of $\approx 0.3 \mu\text{m}$, which is consistent with a Debye length $\lambda_D \equiv (kT_e/4\pi n_e e^2)^{1/2}$ of an electron cloud at a typical density of

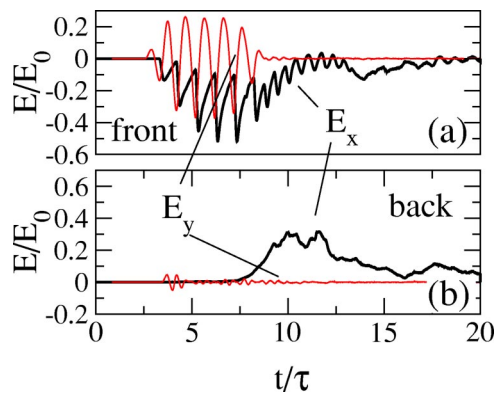


FIG. 4. (Color online). Helium target under oblique incidence. Temporal evolution of the electric field components E_x and E_y on the front (a) at $x = 3.0\lambda$, and rear surface (b) at $x = 4.0\lambda$. As soon as some fast electrons leave the target, E_x rises to a level of $0.3E_0$ and stays there for several laser cycles.

$n_e \approx 0.05n_c$ and a typical energy density of $k_B T_e \approx 0.1 m_e c^2 \approx 20$ keV, the values found in our simulation. The charge state distribution in Fig. 3 shows a thin layer of He^{2+} with a thickness of $0.01 \mu\text{m}$; deeper within the target, the dominating charge state is He^+ .

Figure 4 shows the temporal evolution of the longitudinal electric field E_x at front (a) and rear target surface (b). They are recorded in the first and last cells that contain particles initially. As fast electrons pass the target and exit at its rear surface, E_x rises within a few laser cycles and remains then on a high level of the order of 10^{12} V/m for a time period of several laser cycles, see Fig. 4(b). The peak value of this longitudinal field behind the target is of the same order as the maximum laser field amplitude in front of the target, compare Figs. 4(a) and 4(b). The longitudinal electric field on the front surface of the target, as given in Fig. 4(a), is also of the order 10^{12} V/m but, in contrast to the rear side, has an oscillating transverse component due to the field of the laser pulse and the collective motion of electrons with respect to the ions. The E_z component is negligible. Note that Fig. 4(b) also shows the remainder of the front part of the laser pulse that has passed through the target before ionization has set in. Depletion of the pulse energy due to ionization can be seen by comparing the E_y amplitude of the first two periods of the laser pulse as it enters the gas layer, Fig. 4(a), and as it leaves, Fig. 4(b).

It is instructive to compare electron energy spectra of the normal incidence case with that of oblique incidence. The electron spectrum shown in Fig. 5 for time $t = 12\tau$ shows that the fastest electrons in the oblique-incidence case are $\approx 50\%$ more energetic than under normal incidence, giving a higher electric field at the rear surface. This results from the higher coupling efficiency when the laser electric field has a component along the target normal, while under normal incidence fast electrons are accelerated by the $\mathbf{j} \times \mathbf{B}$ force. The electron spectrum can be described by two exponential-like distribution with $T_c \approx 1$ keV and $T_h \approx 20$ keV for oblique incidence, while $T_h \approx 12$ keV for normal incidence. The longitudinal electron phase-space in Fig. 5(b) shows the recirculation of fast electrons through the target, which can outlast the laser pulse many times, see below. Note that the back-

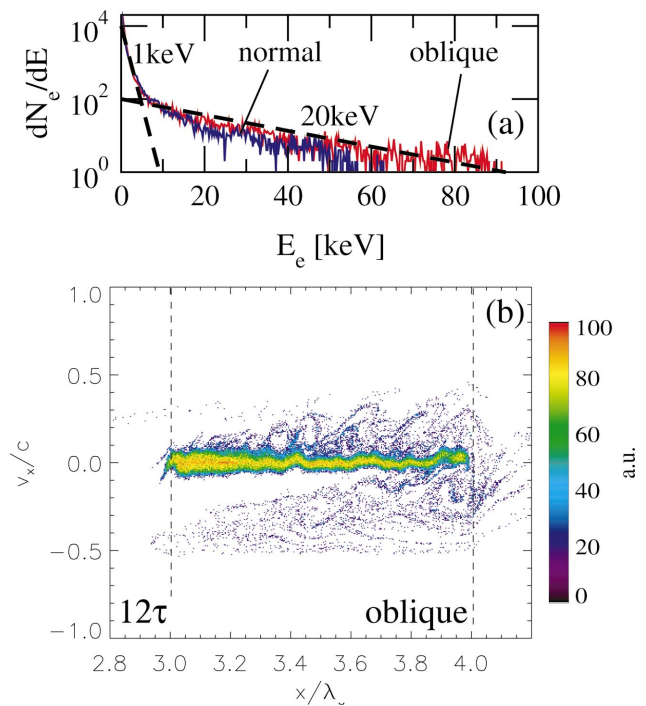


FIG. 5. (Color). Helium target. (a) Energy spectrum of all electrons for normal (blue) and oblique incidence (red). Dashed lines indicate an exponential fit to determine the temperatures given in the viewgraph. (b) Longitudinal phase space of the target electrons after 12 laser cycles for oblique incidence. The boundaries of the target are indicated by vertical dotted help-lines. Colors indicate phase space density.

streaming electrons in the phase plot are more energetic than the forward-streaming because the laser pulse is off for six laser cycles by the time the snapshot is taken.

IV. CASE STUDY: BORON FOIL TARGET

From an experimental point of view, solid targets are easier to realize than the thin gas targets considered so far, and they are more attractive for ion acceleration since their higher electron density results in a shorter Debye length and thus larger electric fields on the target surfaces. As a second model system we now discuss the case of a boron foil target, in part to highlight the extent to which Coulomb collisions modify electron transport through solid targets. The model laser pulse is again six cycles long with a sin-shaped field envelope and a maximum intensity of 10^{18} W/cm² at a wavelength of $\lambda = 395$ nm, corresponding to a frequency-doubled Ti-sapphire laser. Notice that the wavelength is shorter than in the He case, but the $I\lambda^2$ products are comparable. We have chosen the shorter wavelength in this case to be consistent with experimental conditions. Frequency doubling increases the contrast ratio of the laser pulse drastically, which is important for the main pulse to interact with a steep plasma density gradient. The laser pulse impinges (a) normally and (b) obliquely under 31° in order to have a larger conversion of laser energy into fast electrons, as explained in the preceding section. The target thickness is 1λ , its initial ion density is $20n_c$, while the critical density at this wave-

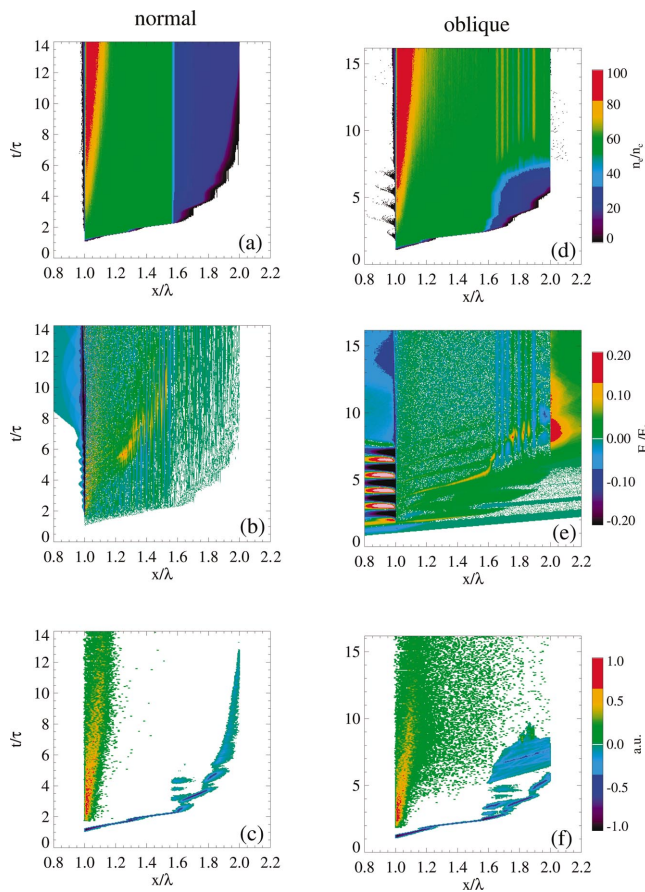


FIG. 6. (Color). Boron foil target under normal (left) and oblique incidence $\alpha=31^\circ$ (right) of laser pulse. (a,d) Electron density n_e in units of the critical density n_c vs target depth x and time t ; (b,e) longitudinal electric field E_x in units of E_0 . (c,f) Ionization events, compare Fig. 1. The laser pulse arrives from the left at the target surface at $t=1\tau$.

length is $n_c=7 \times 10^{21} \text{ cm}^{-3}$. The target material is assumed to be initially neutral, i.e., there are no free electrons and ions are at rest.

Figure 6 shows space-time plots of electron density n_e , the longitudinal field component E_x , and ionization events for normal (left) and oblique incidence (right) of the laser pulse. Similar to the He case, ionization dynamics can be divided into three stages. The first step is field-ionization by the laser pulse. Figure 6(c) presents a space-time history of ionization events due to field and collisional ionization, respectively. Since the boron is not ionized before the arrival of the laser pulse, i.e., there are no free electrons, the first half cycle of the pulse propagates into the foil and field ionizes the front layer up to B^{3+} as soon as the field intensity is strong enough. In a second step, the following half cycles extend this B^{3+} layer and later create a B^+ layer beyond it, which can be identified in the electron density plot as the dark blue region at $x > 1.6\lambda$. The sharp density jump between these layers corresponds to the difference between the field-ionization threshold for the ionization of neutral B and that of B^+ , which is roughly from $4 \times 10^{10} \text{ V/m}$ to $1.5 \times 10^{11} \text{ V/m}$. The transverse laser electric field is able to penetrate deeply into the over critical plasma since the collision frequency in the cold dense plasma is comparable to the

plasma frequency itself, resulting in a collisional de-phasing of the transverse currents that shield the fields out of a collisionless plasma. Field ionization by these collisionally enhanced modes of the laser field is visible in the structure in Fig. 6(c) at times $t > 2\tau$.

In the case of normal incidence, the laser-accelerated electrons from the front have too little energy to penetrate deeper into the target than up to $x=1.6\lambda$. They are mostly stopped in the ionized front layer, which is the reason for the vertical band structure at $x=1.6\lambda$ in Fig. 6(a). On the other hand, in the case of oblique incidence, the laser interaction generates fast electrons via resonance absorption that make collisional ionization deep in the target, shown in Fig. 6(f), and electrostatic waves that are reflected at the electron density jump either at the ionization front or at the target rear surface. The corresponding interference pattern is visible as the vertical bands in both the electron density and longitudinal electric field. In a third step, fast electrons generate space-charge fields behind the target, see Fig. 6(e) at $t=7\tau$. At a magnitude of up to 10^{12} V/m these fields can ionize boron up to B^{3+} and accelerate ions off the target surface.

After the field-ionization wave has passed at $t=2\tau$, material at the front surface is ionized further up to B^{5+} not by the laser field, but by electron collisional ionization. Figures 6(c) and 6(f) show that there are almost no field-ionization processes at the front surface after the first half cycle has passed ($t > 1.4\tau$), but many collisional-ionization events. After the laser has generated the first free electrons via field ionization, they oscillate in the laser field and collisionally ionize the material to higher charge states. As the laser pulse deposits energy to the electrons at the critical surface, diffusive electron energy transport into the target goes along with an ionization front slowly increasing the thickness of the B^{5+} layer to $x < 1.1\lambda$, the dark red area in Figs. 6(c) and 6(f).

Figure 6(e) shows the longitudinal electric field of fast laser-accelerated electrons as they propagate from the front target surface into the foil and exit at the rear surface at $t > 6.3\tau$. These electrons are hardly visible in the space-time history plot, Fig. 6(d), since their density is very low. They exit the foil in bunches, so-called jets, which can also be identified by their longitudinal electric field E_x in Fig. 6(e); they are clearly visible in the longitudinal phase space plot, Fig. 8(b). The first jet that finally reaches the rear side starts at $x=\lambda$, $t=3.5\tau$, passes the B^{3+} layer and enters the B^+ layer at $x=1.6\lambda$, $t=5.2\tau$. The longitudinal electric field build-up in this region is clearly visible. The increasing electron density in this part of the foil ($1.6\lambda < x < 2.0\lambda$) is correlated with the further increasing longitudinal field, see Fig. 6(f) for the corresponding field ionization processes. Figures 6(c) and 6(f) also show the bigger role of collisional ionization as compared to the He target. In addition to being the only available ionization mechanism in the bulk target where the laser cannot penetrate after the target is ionized, collisional ionization is responsible for the high electron density at the critical surface where the laser is absorbed.

Figure 7 shows a snapshot of the longitudinal field E_x at $t=8\tau$. The space-charge separation fields within the foil, seen at ($1.6\lambda < x < 2.0\lambda$) reach $0.75 \times 10^{12} \text{ V/m}$ or 30% of the maximum laser field amplitude. At the rear side, 1.6

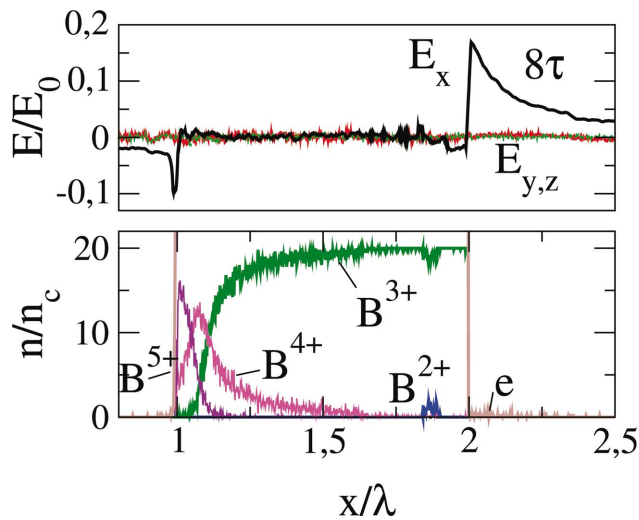


FIG. 7. (Color). Boron target under oblique incidence. Snapshot of electric field and charge state distribution vs target depth x at time $t=8\tau$ corresponding to the maximum value of E_x behind the target.

$\times 10^{12}$ V/m or 60% of the maximum amplitude can be observed. The rear side electric field is—like in the He case—mostly longitudinal; transverse field components are negligible. At the front surface, the temporal structure of the electric fields is qualitatively the same as in the case of the helium gas layer. The longitudinal electric field at the rear target surface is strong enough to remove a few atoms from the rear side of the foil within a few laser cycles and accelerate them into vacuum. The maximal field strength atoms are exposed to is $\approx 10^{12}$ V/m or 44% of the maximal laser amplitude. We have verified numerical convergence of this result by increasing the number of particles per cell by a factor five; the resulting value of E_x differs by less than 10% from the original value.

Figure 8 shows the electron energy spectrum and their longitudinal phase space at eight laser cycles, when the electric field behind the target has reached its maximum. The electron energy spectra resemble the He case, compare Fig. 5(a). The temperature of the cold electron population is almost the same as in the He case, only there is a smaller contribution of fast particles under normal incidence; this can be explained by the steep density gradient at the front of the boron target.²¹ Similar to the phase plot for the He case, shown in Fig. 5(b), one can see the jets of fast electrons penetrating the target and the onset of electron recirculation in Fig. 8(b). The enhanced width of the electron distribution at the rear target surface corresponds to the field ionization that is induced by the space charge of recirculating electrons.

The central difference between solid and gas target is the higher electron density in the solid target. Here we have $n_e^B = 4.2 \times 10^{23} \text{ cm}^{-3}$ for the predominant charge state B^{+3} , as compared to $n_e^{\text{He}} = 4 \times 10^{21} \text{ cm}^{-3}$, at a typical electron temperature of ≈ 100 eV which is comparable in both cases, see Figs. 5, the collision times are $\tau_e^{\text{He}} = 1 \times 10^{-14} \text{ s}$ and $\tau_e^B = 7 \times 10^{-17} \text{ s}$ respectively;⁴⁴ this is the reason why we can neglect collisions in the case of a gas target, as discussed in Sec. III A above.

Energy is conserved to a high degree in the simulation;

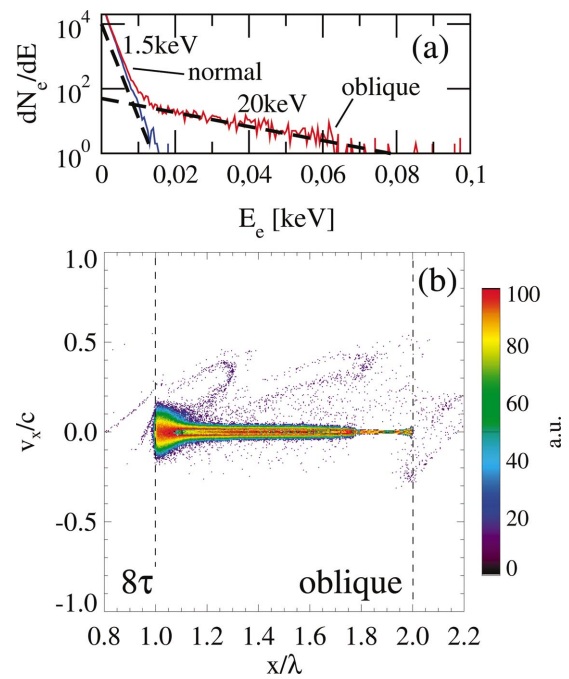


FIG. 8. (Color). Boron target. (a) Energy spectrum of all electrons for normal (blue) and oblique (red) incidence. (b) Longitudinal electron phase space at time $t=8\tau$ for oblique incidence. The target boundaries are indicated by vertical dotted helplines. Colors indicate phase space density.

the code keeps track of the ratio of the relative change of the total energy in the simulation box, and we find that this quantity is conserved to 10^{-6} up to time $t=12\tau$. Note that at this time around 7% of the total energy is in field ionization and 12% in collisional ionization. The total run time of a simulation including the full MCC package for boron is only ≈ 3 times larger than that of a corresponding collisionless simulation with no ionization physics for B^{+3} .

A. Application to ion acceleration

As we have seen above, the electrostatic field at the rear surface outlasts that of the laser pulse even at low laser intensities and pulse lengths. Using a longer laser pulse leads to quasistatic longitudinal electric fields that prevail significantly longer than the laser pulse itself.^{41,45,46} These fields are sustained by the recirculation of the fast electrons through the target which is visible in the simulations presented above, compare Sec. III B. Once an electron is reflected by the electric field behind the target and returns, it crosses the target to the front and the process repeats until (i) the geometric divergence of the electrons rarefies them in the lateral direction (cannot be seen in a 1D simulation), (ii) the longitudinal expansion of the plasma cools them adiabatically, or (iii) their initially directed motion is thermalized by collisions with electrons or ions. The rate at which the latter occurs depends on the collision frequency of the electrons with the background plasma. In our simulation, the effective electron temperature drops by roughly 5–10 keV in the 12 laser cycles after the maximum shown in Fig. 5. Collisional cooling (iii) dominates at low laser intensities and correspondingly small electron energies where Coulomb cross sections are large, compare Fig. 5. In this case, the omission

of collisions and ionization dynamics thus leads not only to the “wrong” ionization states, but also to an overestimation of the longitudinal electric field behind the target. In the case of the boron foil target simulation presented above, where the laser intensity is roughly 10^{18} W/cm², the difference between a collisional simulation and a collisionless one with B^{+3} is roughly 50% in terms of the electric field. At higher laser intensities, e.g., 6×10^{19} W/cm², this difference becomes negligible for $Z=1$ and reduces to values below 20% for $Z=10$. In recent experiments, collimated ion beams from the rear surface of laser-irradiated targets have been observed at a surprisingly low beam emittance and maximum ion kinetic energies in the hundred-MeV range.⁴⁷ Once the generated ion spectrum can be controlled, laser-ion acceleration will have many applications for ion sources in particle accelerators or imaging techniques.^{48,49}

V. SUMMARY

For an adequate description of short-pulse laser-matter interaction at subrelativistic laser intensities, one needs to account for both ionization effects and particle collisions in a kinetic model. The present work addresses these issues by including field and collisional ionization, as well as binary Coulomb collisions between charged particles in a one-dimensional particle-in-cell code. To demonstrate the capabilities of the LPIC-MCC code, we have investigated the interaction of an ultrashort laser pulse with a thin layer of neutral He gas and a thin solid boron foil target as simple model systems; as an application, we have discussed the fast-electron induced ionization dynamics on the rear target surface, and the strong, quasistatic longitudinal electric fields that are generated by fast electrons exiting from the target. These fields are also responsible for the so-called sheath-field acceleration of ions from laser-irradiated foil targets. We are currently implementing our MCC model into a 3D PIC code²³ for a treatment of more complex problems in the future.

ACKNOWLEDGMENTS

A.K. thanks H. Ruhl and Y. Sentoku (UNR) for helpful discussions.

This work has been supported in part by Grant No. KE866 of the Deutsche Forschungsgemeinschaft.

¹T. Brabec and F. Krausz, Rev. Mod. Phys. **72**, 545 (2000).

²M. Perry and G. Mourou, Science **264**, 917 (1994).

³E. Clark, K. Krushelnick, M. Zepf *et al.*, Phys. Rev. Lett. **85**, 1654 (2000).

⁴R. Snavely, M. Key, S. Hatchett *et al.*, Phys. Rev. Lett. **85**, 2945 (2000).

⁵M. Tabak, J. Hammer, M. Glinsky *et al.*, Phys. Plasmas **1**, 1626 (1994).

⁶A. Kemp, Y. Sentoku, T. Cowan, J. Fuchs, and H. Ruhl, Phys. Plasmas **11**,

L69 (2004).

⁷J. Fuchs, T. Cowan, P. Audebert *et al.*, Phys. Rev. Lett. **91**, 255002 (2003).

⁸R. Pfund, Ph.D. thesis, TU München, 1999.

⁹K. Eidmann, J. Meyer-ter-Vehn, T. Schlegel, and S. Hüller, Phys. Rev. E **62**, 1202 (2000).

¹⁰S. Ethier and J. Matte, Phys. Plasmas **8**, 1650 (2001).

¹¹A. Zhidkov and A. Sasaki, Phys. Rev. E **59**, 7085 (1999).

¹²D. Bruhwiler and D. Dimitrov, Phys. Plasmas **10**, 2022 (2003).

¹³C. Birdsall, IEEE Trans. Plasma Sci. **19**, 65 (1991).

¹⁴J. Wallace, D. Forslund, J. Kindel *et al.*, Phys. Fluids B **3**, 2337 (1991).

¹⁵T. Takizuba and H. Abe, J. Comput. Phys. **25**, 205 (1977).

¹⁶R. Town, A. Bell, and S. Rose, Phys. Rev. E **50**, 1413 (1994).

¹⁷A. Kemp, R. Pfund, and J. Meyer-ter-Vehn, “Isochoric heating of solid density matter by ultrashort laser pulse, particle-in-cell-Monte-Carlo simulations” (in preparation).

¹⁸C. Birdsall and A. Langdon, *Plasma Physics via Computer Simulation* (Adam Hilger, New York, 1991).

¹⁹R. Pfund, R. Lichters, and J. Meyer-ter-Vehn, in *Superstrong Fields in Plasmas*, edited by G. Mourou, F. Pegoraro, and E. Sindoni, AIP Conf. Proc. No. 426 (AIP, Woodbury, NY, 1998), p. 141.

²⁰A. Bourdier, Phys. Fluids **26**, 1804 (1983).

²¹Kruer, *The Physics of Laser Plasma Interactions* (Addison-Wesley, Redwood City, CA, 1987).

²²H. Ruhl (private communication).

²³H. Ruhl, Plasma Sources Sci. Technol. **11**, A154 (2002).

²⁴A. Saemann, K. Eidmann, I. E. Golovkin *et al.*, Phys. Rev. Lett. **82**, 4843 (1999).

²⁵V. Tikhonchuk, Phys. Plasmas **8**, 1416 (2002).

²⁶M. Ammosov, N. B. Delone, and V. P. Krainov, Sov. Phys. JETP **64**, 1191 (1986).

²⁷B. Penetrante and J. Bardsley, Phys. Rev. A **43**, 3100 (1991).

²⁸S. Rae and K. Burnett, Phys. Rev. A **46**, 1084 (1992).

²⁹P. Mulser, F. Cornolti, and D. Bauer, Phys. Plasmas **5**, 4466 (1998).

³⁰H. Tawara and T. Kato, “Total and partial ionization cross sections of atoms and ions by electron impact” (unpublished).

³¹W. Lotz, Z. Phys. **232**, 101 (1970).

³²C. Jacoboni and L. Reggiani, Rev. Mod. Phys. **55**, 645 (1983).

³³V. Vahedi and M. Surendra, Comput. Phys. Commun. **87**, 179 (1995).

³⁴K. Aichele *et al.*, J. Phys. B **34**, 4113 (2001).

³⁵Y. Zel’dovich and Y. Raizer, *Physics of Shock Waves and High Temperature Hydrodynamic Phenomena* (Academic, New York, 1967).

³⁶S. Atzeni and J. Meyer-ter-Vehn, *The Physics of Inertial Fusion* (Oxford University Press, Oxford, UK, 2004).

³⁷Y. Sentoku *et al.*, J. Phys. Soc. Jpn. **67**, 4084 (1998).

³⁸R. Shanny, J. Dawson, and J. Greene, Phys. Rev. **17**, 1281 (1967).

³⁹L. Spitzer and R. Härm, Phys. Rev. **89**, 977 (1953).

⁴⁰*Numerical Recipes in C++*, 2nd ed., edited by W. Press *et al.* (Cambridge University Press, Cambridge, UK, 2002).

⁴¹S. Hatchett, C. Brown, T. Cowan *et al.*, Phys. Plasmas **7**, 2076 (2000).

⁴²M. Tatarakis, J. R. Davies, P. Lee *et al.*, Phys. Rev. Lett. **81**, 999 (1998).

⁴³F. Brunel, Phys. Rev. Lett. **59**, 52 (1987).

⁴⁴D. Book, *NRL Plasma Formulary* (Naval Research Laboratory, Washington, DC, 1990).

⁴⁵Y. Sentoku, T. Cowan, A. Kemp, and H. Ruhl, Phys. Plasmas **10**, 2009 (2003).

⁴⁶A. Mackinnon, Y. Sentoku, P. Patel *et al.*, Phys. Rev. Lett. **88**, 215006 (2002).

⁴⁷T. Cowan, J. Fuchs, H. Ruhl *et al.*, Phys. Rev. Lett. **92**, 204801 (2004).

⁴⁸M. Hegelich, S. Karsch, G. Pretzler *et al.*, Phys. Rev. Lett. **89**, 085002 (2002).

⁴⁹M. Allen, Y. Sentoku, P. Audebert *et al.*, Phys. Plasmas **10**, 3283 (2003).